Journal of Materials Chemistry A

ROYAL SOCIETY OF CHEMISTRY

PAPER

View Article Online
View Journal | View Issue

Cite this: *J. Mater. Chem. A*, 2025, **13**, 34730

Delineating the kinetic limitations of $Mn^{2+/3+}$ redox in $LiMn_xFe_{1-x}PO_4$ cathodes for lithium-ion batteries

Seth Reed and Arumugam Manthiram *

Received 23rd July 2025
Accepted 10th September 2025

DOI: 10.1039/d5ta05970d

rsc.li/materials-a

$LiMn_xFe_{1-x}PO_4$ (LMFP) cathodes offer higher energy density than $LiFePO_4$ due to a higher operating voltage. However, the kinetic limitations of the $Mn^{2+/3+}$ redox couple in LMFP restrict its practically achievable capacity and hinder the ability to achieve high energy density. While the shortcomings of $Mn^{2+/3+}$ redox are recognized, its behavior and the factors that impact it remain to be fully understood. We present here an in-depth kinetics study of LMFP by utilizing novel techniques, such as chronoamperometry and galvanostatic electrochemical impedance spectroscopy. Compared to moderate-Mn LMFP (40–60% Mn), high-Mn LMFP (80% Mn) experiences reduced capacity, poor rate capability, and heightened impedance during $Mn^{2+/3+}$ redox. The oxidation of Mn^{2+} to Mn^{3+} becomes more resistive during charge due to the formation of Jahn–Teller active Mn^{3+} and the increasing charge-transfer insulating behavior of $Mn_xFe_{1-x}PO_4$. However, the impedance associated with Mn^{3+} to Mn^{2+} reduction remains constant during discharge in the entire region. The protracted Mn^{2+} oxidation in high-Mn LMFP results in excessive impedance compared to that in moderate-Mn LMFP, even at low C-rates and high cycling temperatures. Despite the promise of high energy density, the extreme kinetic limitations inherent to high-Mn LMFP present a barrier.

Introduction

$LiFePO_4$ (LFP) is a cost-effective option among cathodes for lithium-ion batteries (LIBs).[1–3] In addition to its low cost of production, LFP with the olivine structure is chemically stable, enabling long cycle life.[3,4] However, its low capacity (160 mA h g^{-1}) and discharge potential (3.4 V *vs.* Li/Li^+) result in low energy density when compared to other LIB cathode compositions, such as high-Ni $LiNi_{1-y}Mn_xCo_yO_2$ (NMC).[4–6] While the layered oxide cathodes provide superior discharge capacity and high discharge potential, Ni and Co are critical elements, whose scarcity severely increase the cost of the cathode. Therefore, NMC-based LIBs are expensive even when normalized to energy (*i.e.*, $ per kWh).[7] To minimize the cost of LIBs, the energy density of the cathode must surpass LFP without relying on critical elements or expensive processing approaches. One approach to achieve this is by doping Mn into LFP to form $LiMn_xFe_{1-x}PO_4$ (LMFP).[1,8–11] Because the voltage plateau of the $Mn^{2+/3+}$ redox couple (4.0 V *vs.* Li/Li^+) is higher than that of $Fe^{2+/3+}$ redox, the energy density of LMFP can theoretically be increased by 15% compared to that of LFP.

However, increasing Mn content significantly in LMFP has been observed with a decrease in the practical capacity.[8,10,12] This result is rooted in the Jahn–Teller distortion, a phenomenon which occurs when Mn^{3+}: $t_{2g}^3e_g^1$ is produced during charge. As charging proceeds and more Mn^{3+} is formed, the anisotropic lattice distortion introduces strain, which hinders Li^+ diffusion.[13,14] As a result, the kinetic limitations of the $Mn^{2+/3+}$ redox couple significantly reduce the practical capacity that can be obtained. Because of this, the end member $LiMnPO_4$ is not a suitable cathode since $Mn^{2+/3+}$ redox is the only reaction occurring. Therefore, $LiMnPO_4$ achieves only ~50% of its theoretical capacity.[10,15] Because Jahn–Teller distortion is innate to LMFP, synthesis procedures have been developed to minimize the detrimental impacts of the phenomenon. From nanosizing the cathode material to implementing various dopants, the electrochemical performance of LMFP, including high-Mn LMFP, could be improved.[16–19] While these approaches have helped overcome the slow Li^+ diffusion and lattice strain, the nature and impact of the $Mn^{2+/3+}$ redox kinetics in LMFP needs to be fully understood.

Therefore, the fundamental behavior of the $Mn^{2+/3+}$ redox couple needs further investigation. *Operando* measurements can specifically probe the formation of Jahn–Teller active Mn^{3+}. Previous studies have conducted *in situ* X-ray diffraction on LMFP cathodes with various compositions to examine the lattice parameter changes during charge/discharge.[14,16,18,20] The pathway of lithiation/delithiation reactions during $Fe^{2+/3+}$ and $Mn^{2+/3+}$ redox couples have been shown to vary depending on the molar ratio of Fe and Mn in LMFP. When investigated separately as $LiFePO_4$ and $LiMnPO_4$, the redox reactions in both

Materials Science and Engineering Program, Walker Department of Mechanical Engineering, The University of Texas at Austin, Austin, Texas 78712, USA. E-mail: manth@austin.utexas.edu

cathodes undergo a two-phase reaction as indicated by flat voltage plateaus and discrete changes in the unit cell volume.[21–23] In contrast, for LMFP with <40% Mn, the $Mn^{2+/3+}$ redox reactions proceed as a solid solution reaction indicated by a sloping voltage region centered around 4.0 V and gradual changes in the unit cell volume.[9] By choosing LMFP with low Mn content, the kinetics of $Mn^{2+/3+}$ redox has been improved by avoiding the volume misfit of the LMFP lattice associated with a two-phase reaction. Even though suppressing the transformation strain improves the electrochemical performance of LMFP, $Mn^{2+/3+}$ redox in high-Mn LMFP invariably experiences a sluggish two-phase reaction. While optimizing low-Mn LMFP is important for improved electrochemical performance, understanding the limitations of the two-phase $Mn^{2+/3+}$ redox reactions in high-Mn LMFP can enable development of LMFP compositions with optimal energy density.

In this study, the kinetics of the $Mn^{2+/3+}$ redox couple in LMFP is investigated by taking advantage of distinct electrode choices and kinetic testing procedures. LMFP with 40% Mn, 60% Mn, and 80% Mn, which are hereafter referred to as, respectively, LMFP-40, LMFP-60, and LMFP-80, are investigated. Chronoamperometry rate testing and *operando* galvanostatic electrochemical impedance spectroscopy (GEIS) are implemented to assess and understand the resistive behavior of LMFP cathodes, specifically focusing on the $Mn^{2+/3+}$ redox couple. Mn content, operating temperature, and C-rate are all varied to understand the limitations of this reaction. The environment of LMFP during $Mn^{2+/3+}$ redox, both chemically and environmentally, have distinct impacts on the kinetics of this redox couple. While the adjustment of certain external parameters can reduce the resistance associated with the reaction, high-Mn LMFP (*i.e.*, LMFP-80) exhibits significantly high impedance that cannot be mitigated to match that of moderate-Mn LMFP (*e.g.*, LMFP-40 and LMFP-60). Therefore, the application of high-Mn (~80% Mn) LMFP cathode systems may need reconsideration.

Experimental

Materials preparation

To synthesize LMFP, $NH_4Mn_xFe_{1-x}PO_4 \cdot H_2O$ was used as the Mn and Fe source with $x = 0.4$, 0.6, and 0.8. This precursor was synthesized through a co-precipitation reaction described in a previous publication.[11] To reiterate, the metal solution (250 mL) contained 0.60 M, 0.40 M, or 0.20 M $FeSO_4 \cdot 7H_2O$ (98%, Themo Scientific) mixed with, respectively, 0.40 M, 0.60 M, or 0.80 M $MnSO_4 \cdot H_2O$ (99+%, Thermo Scientific) in addition to 1.00 M H_3PO_4 (ACS reagent, Sigma-Aldrich). The base solution (100 mL) contained 5.00 M NH_4OH (Certified ACS Plus, Fisher Chemical). A 2 L reaction vessel was initially filled with 350 mL of a solution containing 0.07 M H_3PO_4 and 0.07 M NH_4OH. The metal and base solutions were added dropwise to the reaction vessel with a peristaltic pump at flow rates of, respectively, 3.63 and 1.43 mL min^{-1}. A solution temperature of 65–85 °C, a pH of 8, and continuous stirring at 450 rpm were maintained during the reaction. The reaction temperature was altered depending on the Mn content of the LMFP precursor due to the low K_{sp} of $FePO_4$ compared to that of $MnPO_4$. Higher temperature is needed for LMFP precursors containing low Mn content (high Fe content) to promote the formation of the Mn/Fe mixed phase and to avoid the formation $FePO_4$ due to phase segregation. After cooling, the precipitated product was filtered and washed with deionized H_2O. The product was completely dried at 110 °C under vacuum overnight.

Utilizing this precursor, three separate LMFP samples were prepared with each of the $NH_4Mn_xFe_{1-x}PO_4 \cdot H_2O$ precursors ($x = 0.4$, 0.6, and 0.8). For simplicity, the cathode samples will be referred to as LMFP-40, LMFP-60, and LMFP-80, respectively, for $Li_{1.05}Mn_{0.38}Fe_{0.58}V_{0.02}Mg_{0.01}Co_{0.01}(PO_4)_{1.02}$, $Li_{1.05}Mn_{0.57}Fe_{0.37}V_{0.02}Mg_{0.03}Co_{0.01}(PO_4)_{1.02}$, and $Li_{1.05}Mn_{0.76}Fe_{0.16}V_{0.02}Mg_{0.05}Co_{0.01}(PO_4)_{1.02}$. Additionally, each sample had a nominal carbon content of 5 wt%. The carbon content was confirmed by thermogravimetric analysis (TGA) and explained later in detail. Co is an effective transition-metal catalyst for the graphitization of carbon and is included to promote the formation of a uniform and conductive carbon coating on LMFP.[24] V addition in LMFP synthesis forms $Li_3V_2(PO_4)_3$, which exhibits fast Li-ion diffusion and helps improve the low ionic diffusion of LMFP.[25] The Mg content, y, varied respective to the Mn content. Mg is known as a pillaring dopant, helping widen the channels of Li^+ diffusion along the *b*-axis.[26] Mg has also been shown to help $Fe^{2+/3+}$ and $Mn^{2+/3+}$ redox couples behave more as solid solution reactions.[10] Due to these benefits of doping Mg into LMFP, it was concluded that increasing Mg-content directly with Mn-content would produce the best performing material at each Mn composition. Therefore, the resulting doped LMFP cathodes had 1 mol% Mg substituted into LMFP-40, 3 mol% Mg substituted into LMFP-60, and 5 mol% Mg substituted into LMFP-80. To synthesize LMFP, the $NH_4Mn_xFe_{1-x}PO_4 \cdot H_2O$ precursor was combined with Li_2CO_3 (Sigma-Aldrich, ACS reagent), $NH_4H_2PO_4$ (Sigma-Aldrich, 98.5%), $CoC_2O_4 \cdot 2H_2O$ (Thermo Scientific, reagent grade), $MgC_2O_4 \cdot 2H_2O$ (Alfa Aesar, 98.5%), and NH_4VO_3 (Acros Organics, 98%) in stoichiometric amounts that match the nominal molar composition for each LMFP sample. To form a carbon coating on the LMFP particles, a 70 : 30 weight percent ratio of, respectively, lactose (ChemCenter, reagent grade) and maltodextrin (Sigma-Aldrich, dextrose equivalent 4.0–7.0) was used. Carboxymethyl cellulose (CMC) (Nippon Paper, Sunrose MAC Series) was added to the solution as a dispersant. For example, for LMFP-60, 0.056 mol of $NH_4Mn_{0.60}Fe_{0.40}PO_4 \cdot H_2O$ was mixed with 0.032 mol of Li_2CO_3, 4.79 mmol of $NH_4H_2PO_4$, 0.60 mmol of $CoC_2O_4 \cdot 2H_2O$, 1.80 mmol of $MgC_2O_4 \cdot 2H_2O$, 1.20 mmol of NH_4VO_3, 1.17 g of lactose, 0.50 g of maltodextrin, and 0.33 g of CMC.

The precursors, carbon sources, and water were milled in an 80 mL stainless steel ball mill jar with 70 g of 5 mm diameter stainless steel media with a Fritsch Pulverisette 6 planetary ball mill. Mill time was set to 7.5 h at 450 rpm (30 repetitions of 15 min on, 15 min rest). During this mill step, the viscosity of the milled solution was kept high (~38% solid loading) to ensure efficient milling of the precursors and uniformity of the precursors throughout the solution. Then, the solution was diluted to achieve the optimal viscosity for spray drying. The diluted solution was fed into a Labfreez benchtop spray dryer at

a rate of 2 mL min^{-1} and a solid loading between 23% and 33%. The spray gun was pressurized to 0.15 MPa with air, and the air flow rate through the spray dryer was set at 20 scfm. The inlet temperature was maintained at 125 °C, and the resultant exhaust temperature remained around 62 °C. The collected spray dried product was calcined at 350 °C for 1 h, and then 650 °C for 2 h under Ar flow to form LMFP.

Characterization

The purity of the LMFP samples was confirmed with X-ray diffraction (Rigaku Miniflex). Scans were conducted at 1° per min with Cu K_α radiation. Rietveld refinement analysis was conducted with Rigaku PDXL integrated powder XRD software. Scanning electron microscopy (SEM) examined the morphology of the spray dried secondary particles. SEM images were captured on a Tescan Vega3 SEM. To examine the carbon coating amount on each sample, thermogravimetric analysis (TGA) was conducted with a Netzsch STA 449 F3 Jupiter thermal analyzer. LMFP samples were heated to 700 °C at a heating rate of 5 °C min^{-1} under air flow and then held at 700 °C for 1 h to obtain a steady-state value at this final temperature.

To calculate the carbon amount, proper baseline subtraction for each sample is needed. Calcining LMFP in air will incur two oxidation reactions: (1) the carbon coating will oxidize into CO_2 and off-gas from the cathode material and (2) Fe^{2+} will be oxidized to Fe^{3+} in the form of $FePO_4$ and Fe_2O_3. Mn will remain in its 2+ oxidation state, forming $LiMnPO_4$, while remaining Li will react to form Li_3PO_4.[27] The predicted reaction mechanism is presented in eqn (1):

$$xC + yLiMn_zFe_{1-z}PO_4 + \left(x + \frac{y(1-z)}{4}\right)O_2 \rightarrow yzLiMnPO_4 + \frac{y(1-z)}{3}Li_3PO_4 + \frac{2y(1-z)}{3}FePO_4 + \frac{y(1-z)}{6}Fe_2O_3 + xCO_2 \quad (1)$$

Analyzing the TGA curves, the total mass of the reactants is at a minimum between 200 and 300 °C where all adsorbed water has evaporated from the sample. Similarly, the total mass of the products is achieved at the end of the TGA curve. Utilizing these masses and the molar masses of all solid components in eqn (1), the moles of the carbon and LMFP, denoted respectively by x and y, can be calculated. Furthermore, these can be converted to mass values and used to calculate the weight percent of carbon coated onto each LMFP cathode sample.

Electrochemical examination

All the LMFP samples were cast onto a current collector *via* a slurry casting method. LMFP was dispersed in *N*-methyl-2-pyrrolidone (Sigma-Aldrich, 99.5%) with a conductive carbon mixture of Super C65 (Imerys Timcal) and vapor-grown carbon fibers (Showa Denko) in a 2 : 1 ratio by weight and polyvinylidene fluoride (Kynar HSV1800) binder. The compositions of the active material, conductive carbon, and binder were, respectively, 94 : 3 : 3 by weight. Slurry mixing occurred in an ARV-310 Thinky mixer operated at 2000 rpm. The slurry was cast onto carbon-coated Al foil at an aerial loading between 0.8 and 1.1 mA h cm^{-2}. After casting, the cathode was dried at 110 °C to evaporate all solvent and hot calendared at 110 °C between stainless steel shims to ~1.8 g cm^{-3} press density. Cathodes were stored under vacuum at 110 °C overnight to completely dry the electrode.

To conduct cycle life and rate testing, LMFP cathodes were punched into 1/2 in. diameter discs. 2032-type coin cells were assembled inside an argon-filled glovebox with O_2 and H_2O levels both maintained <0.1 ppm. LP57 electrolyte was used in all cells in this study, which consists of 1.0 M $LiPF_6$ in ethylene carbonate/ethyl methyl carbonate (3 : 7 by weight). Half cells were composed of LMFP as the cathode, 50 μL of LP57 electrolyte, 3/4 in. diameter Celgard 2325 separator, and a 5/8 in. diameter lithium-metal anode. For cycle life testing, LMFP half cells were cycled from 2.0 to 4.3 V *vs.* Li/Li^+ at C/3 rate for 100 cycles after 4 formation cycles at C/10 rate. A constant current/constant voltage charge procedure was used; the current associated with a specified C-rate was applied until 4.3 V was reached. Then, the potential was held at 4.3 V until the current dropped below C/25 rate. The discharge procedure did not include a constant voltage discharge step. Additionally, charge rate testing was conducted with various charge rates followed by a constant C/10 discharge rate. The cells were cycled from 2.0 to 4.5 V without a potential hold at either the end of charge or discharge. Three cycles were conducted at each charge rate. All cycling and charge rate testing were conducted at room temperature, which was maintained approximately at 21 °C, on an Arbin LBT-20084. All elevated cycling temperature testing was performed within an environmental chamber (ESPEC BTZ-133) held at 45 °C.

In order to solely investigate the kinetics of the $Mn^{2+/3+}$ redox couple, symmetric cells were built with LMFP. First, electrode formation for the symmetric cell was carried out within a Swagelok cell assembled inside an argon-filled glovebox. A 5/8 in. diameter pristine LMFP cathode was paired with a 5/8 in. diameter Li-metal anode in the Swagelok cell with 60 μL of LP57 electrolyte. Two separators were used: Celgard 4560 was placed on the anode side, and Celgard 2325 was placed on the cathode side. Including both separators helped prevent cell shorting when the Swagelok cell was disassembled. Both separators were punched to 11/16 in. diameter. Two cells were assembled and charged in an environmental chamber held at 45 °C. One cell was stopped at 3.9 V (after Fe^{2+} oxidation and before the beginning of Mn^{2+} oxidation) and the other cell was stopped at 4.4 V (after Mn^{2+} oxidation, fully delithiated). Charge current was set at C/10 rate. A constant voltage step (maintained until the current dropped below C/25 rate) at each voltage followed this constant current step to ensure that the respective oxidation reaction was fully completed. These cells were disassembled inside an argon-filled glovebox, and the cathodes were washed with dimethyl carbonate (Sigma-Aldrich, anhydrous, >99%) to remove any residual electrolyte components deposited from the formation step. After drying the electrodes, they were paired in a 2032-type coin cell with 40 μL of LP57 electrolyte and 3/4 in. diameter Celgard 2325 separator. A surface-treated Al foil (Toyal Carbo) was placed underneath the

anode (fully delithiated LMFP) to keep electrolyte from contacting the cell case and causing additional impedance. The symmetric cells, therefore, simply scanned the $Mn^{2+/3+}$ redox plateau for both electrodes, and the cells were cycled between −0.5 and 0.5 V.

To deconvolute the impedance caused by Mn^{2+} oxidation and Mn^{3+} reduction, pristine LMFP cathodes were also paired with $Li_4Ti_5O_{12}$ (MSE Supplies, >99%) as the anode. $Li_4Ti_5O_{12}$ (LTO) is known to have low impedance and optimal rate performance, allowing for the impedance of the cathode to be clearly investigated. LTO was cast as an anode following the same slurry casting method as LMFP (94% active material on carbon-coated Al foil). Aerial loading for LTO was maintained around 1.5 mA h cm^{-2}. Coin full cells were composed of 9/16 in. diameter LMFP cathode, 40 μL of LP57 electrolyte, 3/4 in. diameter Celgard 2325 separator, and 5/8 in. diameter LTO anode. These full cells were cycled between 0.5 and 3.0 V *vs.* LTO.

Operando galvanostatic impedance spectroscopy (GEIS) and chronoamperometry were conducted with a VMP3 Biologic potentiostat. Both the *operando* GEIS and chronoamperometry procedures were adapted from previous studies utilizing these techniques.[28,29] Chronoamperometry was conducted by setting the voltage of the symmetric cell to 0.5 V and reading the current and capacity until the current dropped below C/25 rate. The current for *operando* GEIS was set to a various C-rates with a sinus amplitude set to 50% of the applied current. The frequency range for each scan was set between 100 kHz and 90 mHz. With seven data points per decade, each EIS scan took ∼2 min. Scans were repeated until the cutoff voltages were reached. For the LMFP and LTO symmetric cells, the cutoff voltages were 0.5 V for charge and −0.5 V for discharge. For the LMFP‖LTO full cell, the cutoff voltages were 3.0 V for charge and 0.5 V for discharge. After charge or discharge, a 5 min rest and potentiostatic EIS was conducted to examine the impedance at the end of charge and discharge. To account for active material loading variations in the different cells examined, the impedance collected was normalized to the active material mass of the working electrode. For the symmetric cell, the active material mass is the mass of the partially lithiated cathode. For the LMFP‖LTO full cell, the active material mass is the mass of the pristine LMFP cathode.

To examine the direct current resistance response of LMFP symmetric cells, galvanostatic impedance titration technique (GITT) was performed. Current was pulsed at a C/10 rate for 5 min, followed by a rest period of 15 min to allow the cell to return to equilibrium. Current pulses were applied in this continuous loop until the upper cutoff voltage of 0.5 V was surpassed.

Results and discussion

The scanning electron microscopy (SEM) images in Fig. S-1 present the uniform and spherical secondary particles of LMFP-40, LMFP-60, and LMFP-80. Spray drying produces secondary particles with diameters of 3–15 μm for all three samples. The variance in secondary particle sizes is natural to the spray drying process. This optimal particle morphology, as well as varied secondary particle sizes, improves electrode-level packing, allowing for complete electrode utilization and improved electrode compression density. Furthermore, X-ray diffraction (XRD) indicates that all the three LMFP samples are single-phase (Fig. 1a). With Rietveld refinement, unit cell parameters, cell volume, and the weighted profile residual were obtained for the three samples (Fig. S-2 and Table S-1). As expected, unit cell volume increases with Mn content due to the larger ionic radius of Mn^{2+} (0.97 Å) compared to that of Fe^{2+} (0.92 Å).[3,13] In addition to the purity of the active material, the surface carbon coating must also be comparable across all cathode materials. Thermogravimetric analysis (TGA) indicates that the carbon coating for each cathode material is approximately 3.5 wt% (±0.1 wt%) (Fig. 1b). To ensure the validity of eqn (1), XRD was conducted on LMFP-60 following TGA analysis, and the XRD pattern aligns well with the predicted products of the oxidation reaction (Fig. S-3). Thus, all the three LMFP samples are phase-pure, have similar particle morphology, and are coated with a similar amount of carbon. Therefore, this allows for an accurate comparison of the electrochemical data.

The electrochemical performances of LMFP half-cells are impacted by the Mn content in the cathode. The charge–discharge profiles clearly depict the Fe : Mn ratio in each cathode based on the amount of capacity gained from the ∼3.4 V plateau ($Fe^{2+/3+}$ redox) *versus* the ∼4.0 V plateau ($Mn^{2+/3+}$ redox) (Fig. 1c). At higher Mn contents, the cathode gains more capacity at a higher voltage, increasing the energy density of the cathode. However, capacity limitations are more aggressive for LMFP with a higher Mn content. As seen during the constant voltage charging step at the end of the charge profile, the capacity obtained at 4.3 V increases directly with Mn content, reflecting the sluggish $Mn^{2+/3+}$ kinetics at higher Mn contents. When the half-cells are discharged, LMFP-40 achieves the highest capacity, followed by LMFP-60 and LMFP-80 (the least capacity) (Fig. 1c). All the three cathodes exhibit good cycle life (Fig. 1d). To understand the role of the $Mn^{2+/3+}$ redox couple in the cathode, the percentage of total capacity that is contributed by the $Mn^{2+/3+}$ redox was calculated and compared to the theoretical capacity for each LMFP cathode. Fig. 1e presents the fractions of capacity that come from each redox reaction at C/10 rate. As seen, the observed capacity values for the $Mn^{2+/3+}$ redox couple are lower than the expected theoretical capacity. Also, as the Mn content increases, the percentage deviation between the practical and theoretical capacity increases: 3% for LMFP-40, 6% for LMFP-60, and 9% for LMFP-80. Analysis of the discharge profiles illuminates the poor kinetics of the $Mn^{2+/3+}$ redox couple, which is the rate limiting reaction in LMFP when compared to the $Fe^{2+/3+}$ redox couple. Adding more Mn to LMFP exacerbates these limitations. These observations are consistent with previous studies.[8,18]

Rate capability evaluation was then conducted to ascertain the kinetic limitations of the cathode as a function of Mn content. Rate testing is generally conducted with a specific focus on varying the rate of discharge. Thus, rate capability testing studies of LMFP that utilized a constant charge rate and variable discharge rates have demonstrated great rate capability

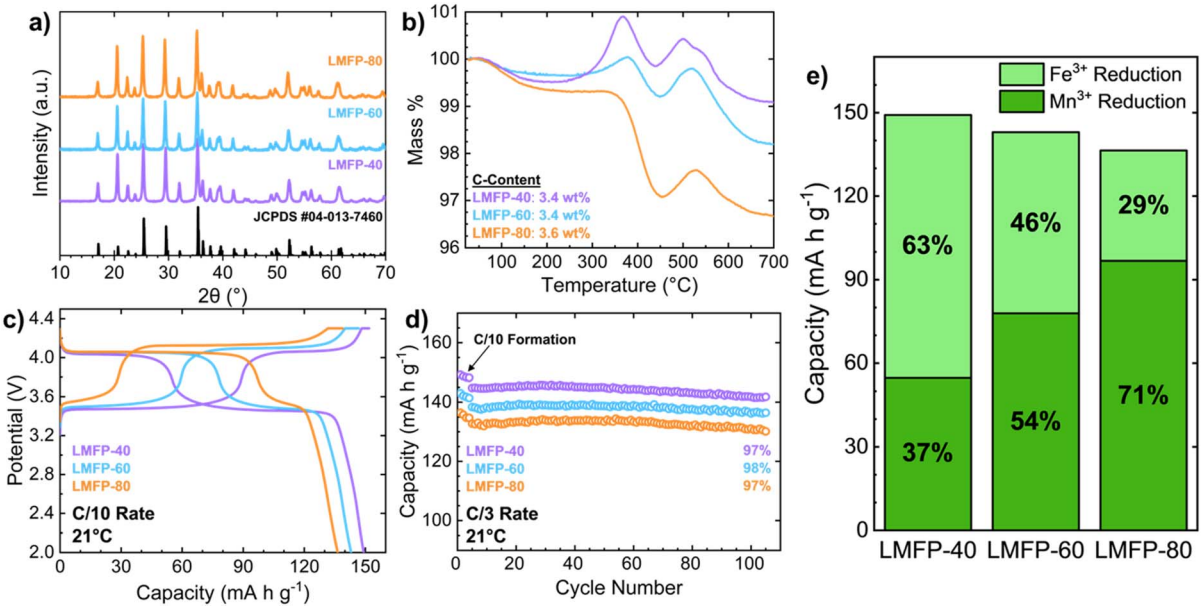

Fig. 1 Physical and electrochemical characterization of LMFP-40, LMFP-60, and LMFP-80. (a) XRD patterns of the LMFP samples in comparison to $LiMn_{0.5}Fe_{0.5}PO_4$ (JCPDS #04-013-7460). (b) TGA profiles with calculated carbon content for each cathode. (c) Charge and discharge profiles at C/10 rate. (d) Cyclability at C/3 rate over 100 cycles. (e) Discharge capacity contributions from Mn^{3+} and Fe^{3+} reduction reactions at C/10 rate.

under high discharge rates (5C–10C rate).[14,30,31] In contrast, rate capability evaluation by varying both the charge and discharge rates display more drastic capacity reduction at high C-rates.[14] This reveals that the delithiation of LMFP is the rate limiting reaction of the cathode, which will be addressed and discussed further. Therefore, charge rate testing (variable charge rate, constant discharge rate) was utilized in this study to elucidate the true kinetic limitations of LMFP cathodes. Increasing the charge C-rate reduces the discharge capacity more significantly for LMFP-80 and LMFP-60 than for LMFP-40 at room temperature (21 °C) (Fig. 2a). Specifically, LMFP-80 sustains a drastic drop in capacity at high C-rates (Fig. 2b). During charge, high C-rates cause the Mn^{2+} oxidation reaction to be cut short when compared to low C-rates. Contrarily, there is an insignificant effect of C-rate on the completion of Fe^{2+} oxidation. When discharged at C/10 rate, most of the capacity loss at high C-rates comes from the $Mn^{2+/3+}$ redox plateau. Fig. S-4 quantifies this capacity loss as a function of charge rate. While the $Mn^{2+/3+}$ redox plateau in LMFP-80 accounts for 71% of the discharge capacity at C/10 rate, only 46% of the discharge capacity comes from the same plateau at 5C rate. Mn content is four times higher than Fe content in LMFP-80, yet it cannot produce a capacity even equal to that of Fe when the C-rate is increased to 5C. The disproportionate kinetics of $Mn^{2+/3+}$ and $Fe^{2+/3+}$ redox reactions at fast C-rates severely reduces the capacity, and thereby the energy density of high-Mn LMFP systems.

To alleviate the kinetic limitations of the cathode, rate capability evaluation was conducted at an elevated temperature of 45 °C. Increasing the temperature of a LIB can improve the ionic diffusion in both the electrolyte and cathode, which can offer an overall benefit to the rate performance of the cell. As expected, all LMFP half cells display an increase in discharge capacity at every charge rate tested when the temperature is increased to 45 °C (Fig. 2c). This especially benefitted LMFP-80, which gained capacity nearly identical to that of LMFP-60 at all charge rates at 45 °C. At a faster 1C rate, increasing the cycling temperature resulted in a commensurate capacity gain of ~28 mA h g^{-1} for LMFP-80, with ~26 mA h g^{-1} stemming from the $Mn^{2+/3+}$ redox plateau (Fig. 2d). Adjusting the cycling temperature improves the utilization of the $Mn^{2+/3+}$ redox couple, enabling high-Mn LMFP to achieve higher capacities. However, both LMFP-60 and LMFP-80 produce a lower discharge capacity compared to LMFP-40 at every charge rate, indicating that this temperature increase does not fully resolve the sluggish kinetics as Mn content increases. Thus, further investigation into the performance-limiting $Mn^{2+/3+}$ redox couple is needed.

To understand the kinetics of the $Mn^{2+/3+}$ redox couple fully, symmetric cells were assembled with a partially delithiated LMFP (to the extent that only the $Mn^{2+/3+}$ redox remains) as the cathode and a fully delithiated LMFP (MFP) as the anode; both electrodes were formed in half cells at 45 °C to easily achieve the desired Li content. This cell setup allows for only the $Mn^{2+/3+}$ redox plateau to be examined. However, the data from symmetric cells for LMFP-40, LMFP-60, and LMFP-80 requires capacity normalization due to the varied Mn contents, and therefore varied charge stored in the $Mn^{2+/3+}$ redox reaction. The cathode for each symmetric cell has a Li content equivalent to the Mn content (for example, $Li_{0.4}Mn_{0.4}Fe_{0.6}PO_4$ for LMFP-40). To account for Li content differences in each cell, the theoretical capacity of LMFP (170 mA h g^{-1}) was multiplied by the fraction of the Li in the cathode. The normalized theoretical

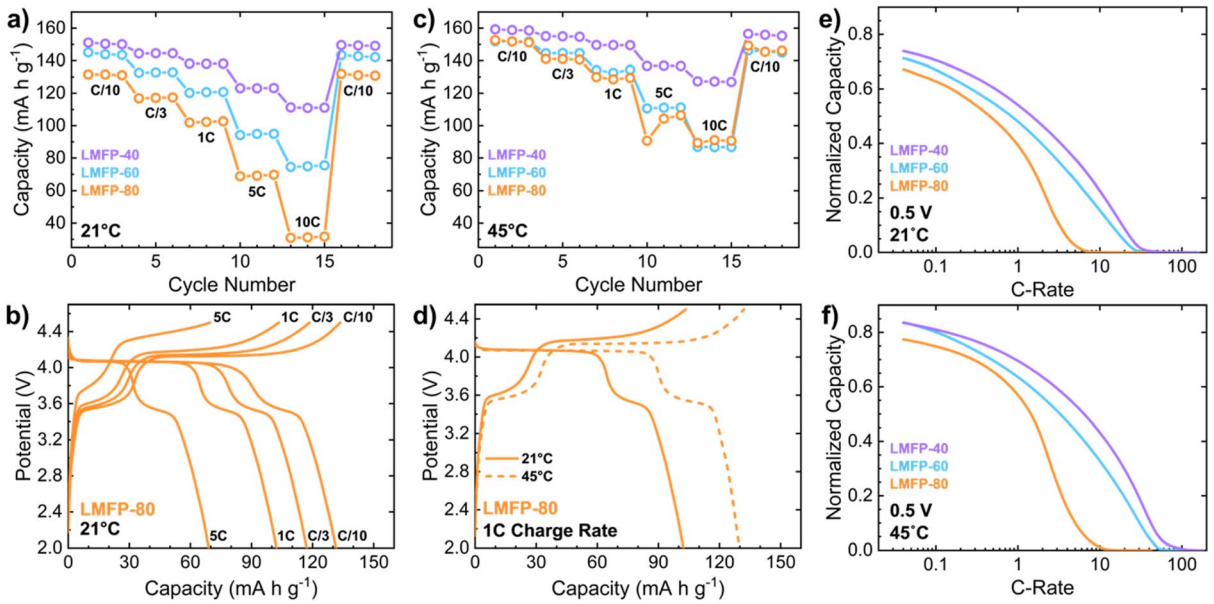

Fig. 2 Rate capability of LMFP-40, LMFP-60, and LMFP-80 at 21 °C and 45 °C. (a) Charge rate testing of LMFP half-cells at 21 °C. The charge rate ranges from C/10 to 10C while the discharge rate is set at C/10. (b) Charge and discharge profiles of LMFP-80 at 21 °C across various charge rates. (c) Charge rate testing of LMFP half-cells at 45 °C. (d) Charge and discharge profiles of LMFP-80 at 21 °C and 45 °C, conducted at 1C charge rate. Chronoamperometry of LMFP symmetric cells conducted at (e) 21 °C and (f) 45 °C.

capacities for LMFP-40, LMFP-60, and LMFP-80 are, respectively, 68, 102, and 136 mA h g^{-1}. It is important to note that the normalized capacity is low for all cells due to factors outside of the restricted kinetics. Nonetheless, since all symmetric cells were assembled with the same procedure, the relative comparisons between cathodes are valid.

Chronoamperometry is an additional rate testing procedure, which includes setting the potential (0.5 V *vs.* MFP) and measuring the current response and capacity gained until a lower cutoff current (C/25 rate) is achieved. Chronoamperometry conducted on symmetric cells reveals the rate capabilities of the $Mn^{2+/3+}$ redox couple. At 21 °C, LMFP-40 achieves the highest normalized capacity across all C-rates, followed by LMFP-60 and LMFP-80 (the least capacity) (Fig. 2e). This trend mimics the data presented for charge rate testing. With a focus on the high current region, the C-rate in which capacity begins increasing indicates the ohmic behavior associated with the activation energy of the redox reaction. Similar to *IR* drop, the current drop associated with the gain in capacity translates to the resistance within the cell. LMFP-40 and LMFP-60 exhibit a minimal gap in C-rate at this point, but there is a large gap between LMFP-60 and LMFP-80. Therefore, the large current drop in LMFP-80 demonstrates a uniquely high resistance of its $Mn^{2+/3+}$ redox reaction. Unlike charge rate testing, chronoamperometry shows that LMFP-80 remains limited by poor rate capability when the cycling temperature is increased to 45 °C (Fig. 2f). The solid solution reaction of Fe^{3+} reduction during charge rate testing could assist in extracting capacity from the Mn^{3+} reduction reaction and improve the performance of LMFP-80 at high temperatures and fast C-rates. However, without $Fe^{2+/3+}$ playing a role in the symmetric cell, the limitations of $Mn^{2+/3+}$ redox cannot be overcome by temperature increase. At the lower cutoff current of C/25 rate, LMFP-40 and LMFP-60 can achieve the same normalized capacity under these kinetically favorable conditions (elevated temperature, low current). However, LMFP-80 is not able to reach the same capacity values at the same conditions. Chronoamperometry, therefore, reveals that $Mn^{2+/3+}$ redox is significantly limited at any current condition in high-Mn LMFP.

Furthermore, the kinetic limitations of LMFP based on Mn content, C-rate, and temperature can be quantified *via operando* GEIS. Previous studies have implemented various EIS procedures to examine the impedance of LMFP.[18,32] However, these tests have been conducted in LMFP half cells with Li metal as the anode. Li metal accounts for nearly all the total impedance of a two-electrode cell when paired with a carbon-coated cathode like LFP or LMFP.[33] Therefore, the true impedance of LMFP cannot be deconvoluted in a half cell, and utilizing a LMFP symmetric cell can begin to resolve this issue. Nyquist plots in Fig. 3 present the results of *operando* GEIS for LMFP-40, LMFP-60, and LMFP-80 at C/10 rate. The impedance is analyzed as trends in the Nyquist plots throughout the $Mn^{2+/3+}$ redox couple. Distribution of relaxation times (DRT) was also conducted on the impedance data for this set of data (Fig. S-5) as an additional analysis method. DRT analysis presents straightforward EIS interpretation as a function of time constants.[34,35] At the beginning of the $Mn^{2+/3+}$ redox couple, the impedance is small for LMFP-40 and LMFP-60. In contrast, the impedance of LMFP-80 is considerably higher than that of LMFP-40 and LMFP-60. For all three cells, the impedance slightly increases with capacity during the voltage plateau. Towards the end of

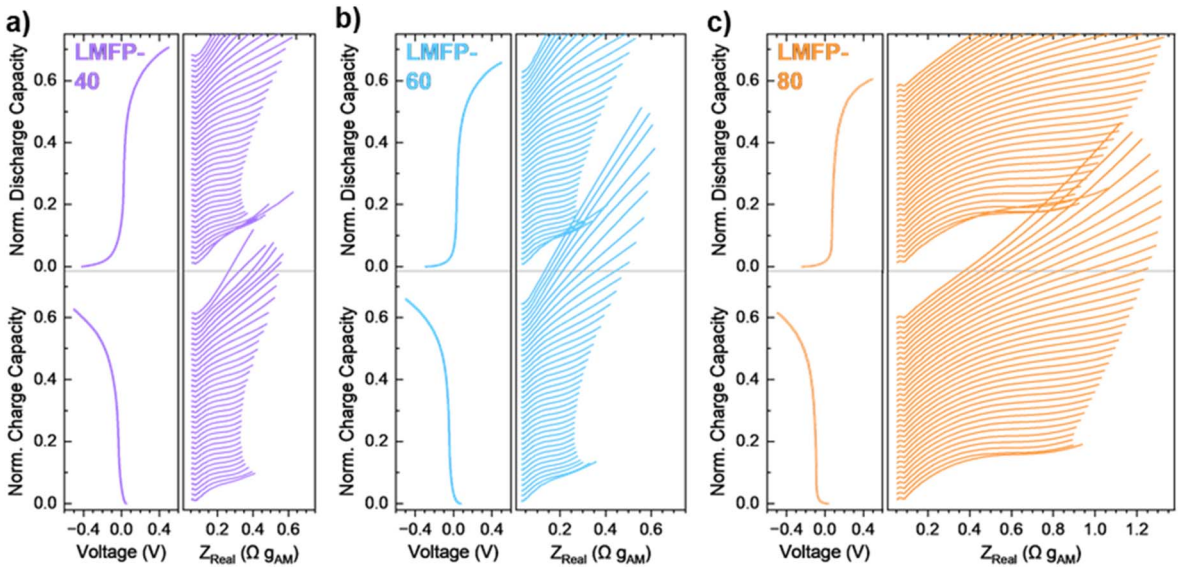

Fig. 3 Nyquist plots of *operando* GEIS conducted on (a) LMFP-40, (b) LMFP-60, and (c) LMFP-80 symmetric cells at C/10 rate and 21 °C.

charge or discharge, the impedance increases drastically as the Li inventory becomes low, and transport limitations dominate. Outside of Mn content, the symmetric cells were also tested at faster C-rates of C/5 and 1C (Fig. S-6). Despite a tenfold increase in current from C/10 to 1C rate, the impedance of $Mn^{2+/3+}$ redox does not significantly increase. In fact, the impedance slightly decreases at 1C rate due to the overpotential increase from the $Mn^{2+/3+}$ redox plateau (Fig. S-7).

Finally, increasing cycling temperature to 45 °C reduces the impedance of the redox reactions in each LMFP symmetric cell across all C-rates (Fig. S-8). As mentioned previously, increasing temperature improves the transport properties of the electrolyte in addition to the kinetics of the $Mn^{2+/3+}$ redox couple, and both have a role in decreasing the impedance. Since the impedance values of LMFP-40 and LMFP-60 are already low at 21 °C, decreasing the temperature brings the impedance to a minimal value. In contrast, LMFP-80 still exhibits significant impedance with a similar rate of increase throughout the reaction, indicating unresolved kinetic limitations in this cathode despite the temperature increase.

While the Nyquist plots present clear impedance trends of each cathode, the differences in the value of impedance across different Mn contents, C-rates, and cycling temperatures are difficult to decipher. Therefore, the impedance value at the end of each scan (90 mHz) is plotted alongside the associated charge profile (Fig. 4). All cathodes do not have well-defined semicircles in the Nyquist plots. Hence, an equivalent circuit model cannot be utilized to calculate the resistance components, such as charge-transfer resistance.[36,37] Instead, the value of impedance was recorded at 90 mHz for each *operando* GEIS scan of all symmetric cells. This moderate frequency probes the kinetic limitations of the electrodes.[36] As displayed in the Nyquist plots, the impedances of LMFP-40 and LMFP-60 are small at the beginning of charge (~0.30 Ω g) and remain constant during the first half of the redox reaction. Then, the impedance slowly increases to surpass 1.00 Ω g by the end of charge (Fig. 4a). The impedance during charge of LMFP-80 begins at 0.90 Ω g, which is similar to the endpoint value of the other cathodes. Also, rather than having steady impedance during the first half of charge, LMFP-80 experiences a linear increase in impedance immediately. By increasing the temperature to 45 °C, the impedances for LMFP-40 and LMFP-60 are cut in half to ~0.17 Ω g (Fig. 4b). Furthermore, the linear increase in impedance during charge becomes minimal for LMFP-60, and the impedance of LMFP-40 remains constant throughout the entirety of charge at 45 °C. In contrast, LMFP-80 has over three times the impedance of the other cathodes (~0.57 Ω g) at the beginning of charge. The increase in impedance during charge remains pronounced and has a slope similar to the impedance increase for LMFP-80 at 21 °C.

The kinetic differences in low-Mn and high-Mn LMFP cathodes can be distinguished by testing LMFP-40 and LMFP-80 at various cycling temperatures. For LMFP-40, applying a low current (C/10 rate) results in low impedance during charge and a drastic decrease in impedance when the cycling temperature is increased to 45 °C (Fig. 4c). At a fast current rate (1C rate), an increase in cycling temperature still provides a similar decline in the impedance for the $Mn^{2+/3+}$ redox couple (Fig. 4d). LMFP-40 possesses the best rate capability of the cathodes examined in this study. The $Mn^{2+/3+}$ redox couple is positively impacted by the increased temperature and is undeterred by the current increase to 1C rate. Similar to LMFP-40, the impedance of LMFP-80 at C/10 rate is positively affected by the increase in cycling temperature to 45 °C (Fig. 4e). However, when the current rate is increased to 1C, the impedance during charge of LMFP-80 is identical at 21 °C and 45 °C (Fig. 4f). Combining high current with high-Mn LMFP creates a kinetically unfavorable environment for the $Mn^{2+/3+}$ redox couple in LMFP-80. As a result, the kinetic limitations of these reactions cannot be alleviated when there is an increase in cycling temperature.

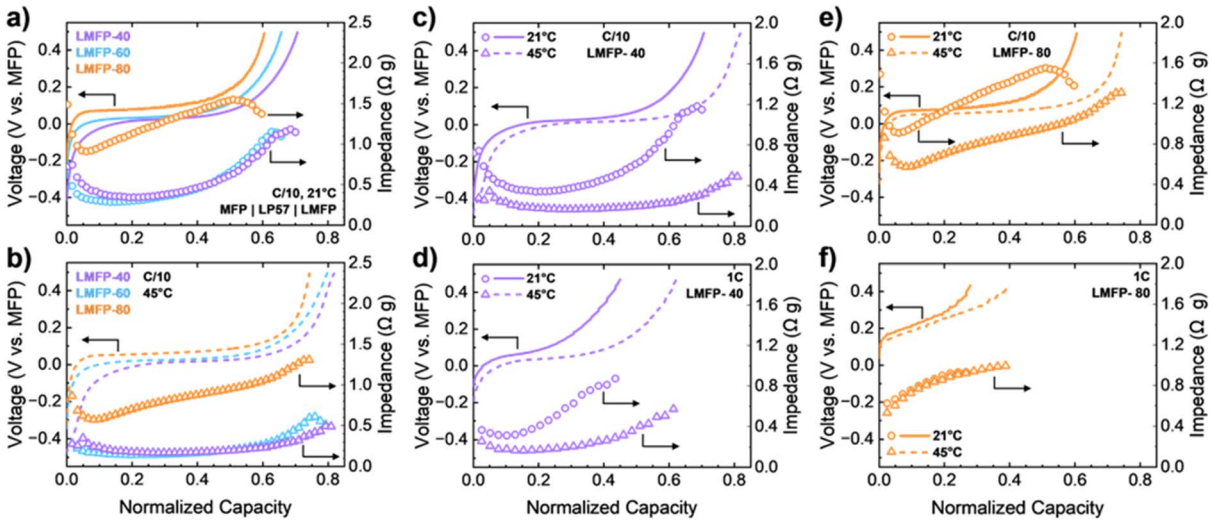

Fig. 4 Impedance of LMFP symmetric cells calculated at 90 mHz during *operando* GEIS, plotted alongside their respective charge profiles. *Operando* GEIS of symmetric cells conducted at C/10 rate at (a) 21 °C and (b) 45 °C. Impact of elevated cycling temperature on LMFP-40 at (c) C/10 rate and (d) 1C rate. Impact of elevated cycling temperature on LMFP-80 at (e) C/10 rate and (f) 1C rate.

LMFP-80 at 45 °C gains slightly more capacity than at 21 °C, however, due to the improved electrolyte transport properties. Overall, the stresses from excessive Jahn–Teller distortion in LMFP-80 at this fast rate need additional assistance (*e.g.*, higher temperatures than 45 °C, slower rate than 1C) to reduce the impedance of its $Mn^{2+/3+}$ redox couple.

Impedance is composed of its real (*i.e.*, resistance) and imaginary (*i.e.*, reactance) parts.[36] Understanding the distribution of the total impedance can further deconvolute the underlying kinetic limitations of these reactions. Across all cells and for both cycling temperatures, the real impedance accounts for nearly all the total impedance (Fig. S-9). Since the real factor of impedance is resistance, assessing the direct current responses of these cells can provide support to the *operando* GEIS data. Specifically, galvanostatic intermittent titration technique (GITT) was conducted with C/10 current pulses (Fig. S-10). The relaxation overpotential increases with Mn content, with a large jump in overpotential from LMFP-40 (18 mV) to LMFP-60 (33 mV) to LMFP-80 (73 mV). This large shift from equilibrium indicates that there is significantly more resistance for the $Mn^{2+/3+}$ redox reaction in LMFP-80.

While the impedance of the $Mn^{2+/3+}$ redox couple is obtained in LMFP symmetric cells, all these measurements account for reactions occurring at both electrodes in the symmetric cell. Moreover, the charge and discharge behaviors of LMFP cannot be deconvoluted since both Mn^{2+} oxidation and Mn^{3+} reduction proceed concurrently. To investigate the difference in impedance growth between oxidation and reduction reactions, pristine LMFP cathodes were paired with an LTO anode to form full cells. *Operando* GEIS was also conducted on an LTO symmetric cell to confirm that the impedance from LTO did not contribute significantly to the total impedance of the LMFP full cell (Fig. S-11). The results show that LTO exhibits minimal, steady impedance throughout its entire redox reaction. This characteristic makes LTO an optimal counter electrode for isolating and analyzing the impedance of LMFP solely. A similar *operando* GEIS procedure was conducted on LMFP full cells at 21 °C, and the impedance at the end of each scan (90 mHz) is plotted alongside the respective charge or discharge profiles (Fig. 5). Nyquist plots were also generated for these three full cells (Fig. S-12). Fe^{2+} oxidation and Fe^{3+} reduction both proceed with a constant, low impedance value (Fig. 5a and c). Since the impedance is constant for both oxidation and reduction reactions of Fe, there are no significant kinetic differences between Fe^{2+} oxidation and Fe^{3+} reduction. Mn^{2+} is present for both reactions of the $Fe^{2+/3+}$ redox couple, which does not present extraneous strain to the lattice. This enables a high-rate capability of the $Fe^{2+/3+}$ redox couple. Interestingly, the impedance of the redox couple increases with Mn content in the cathode: 0.09 Ω g for LMFP-40, 0.12 Ω g for LMFP-60, and 0.17 Ω g for LMFP-80. For LMFP with >50% Mn, the Li^+ diffusion coefficient during $Fe^{2+/3+}$ redox has been calculated to decrease as Mn content increases.[22] One explanation for this trend could be due to the increased energy band gap of LMFP as the Mn content increases.[38,39] Additionally, the increase in the LMFP unit cell volume as Mn content increases also contributes to the impedance increase of the $Fe^{2+/3+}$ redox couple. As a result of lattice expansion, the Fe–O bond in LMFP will stretch further, decreasing the covalence of the Fe–O bond and the electronic conductivity. Both factors contribute to the increase in the impedance of the $Fe^{2+/3+}$ redox couple. Nonetheless, the impedance of $Fe^{2+/3+}$ redox is lower when compared to the $Mn^{2+/3+}$ redox couple across all cells, in line with charge rate testing studies previously conducted. With this understanding, the focus of *operando* GEIS can be solely on the $Mn^{2+/3+}$ redox couple within the full cell.

When Mn^{2+} oxidation begins, all three cathodes have a low value of impedance that is equivalent to that during Fe^{2+} oxidation. However, instead of remaining steady, the impedance increases throughout the entire oxidation reaction

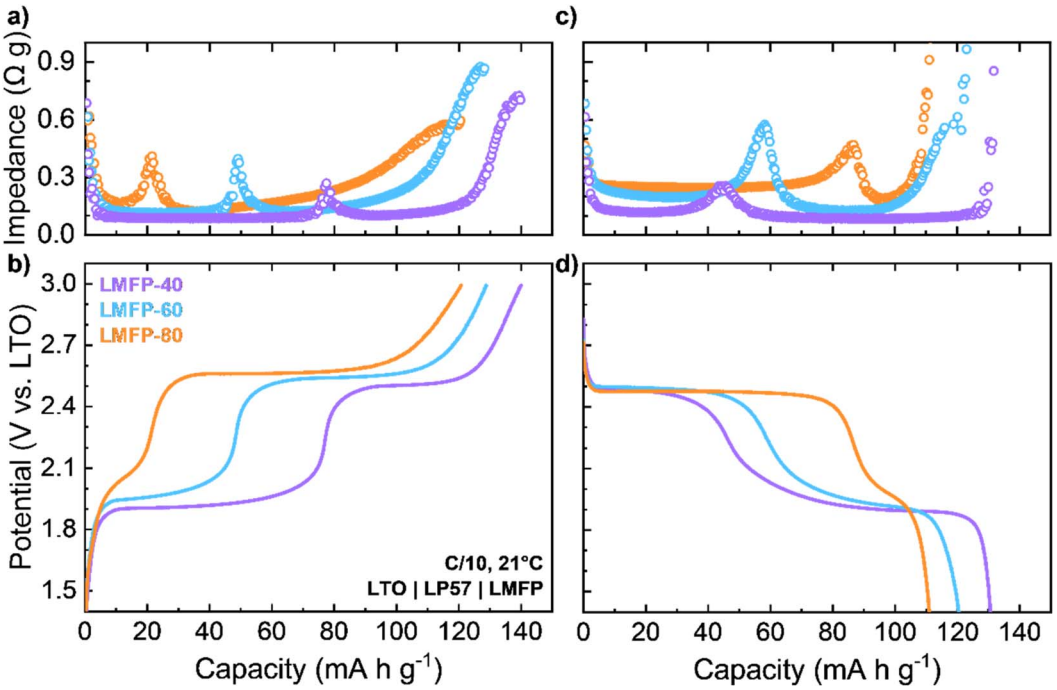

Fig. 5 Charge profiles along with associated (a) impedance and (b) voltage for LMFP-40, LMFP-60, and LMFP-80 during *operando* GEIS of LMFP||LTO full cells conducted at 21 °C and C/10 rate. The respective discharge profiles along with associated (c) impedance and (d) voltage.

(Fig. 5a). The rate of impedance increase becomes more drastic at higher Mn content, similar to the trend discovered in the *operando* GEIS of LMFP symmetric cells (Fig. 4a). Additionally, the LMFP cathodes with higher Mn content undergo Mn^{2+} oxidation for longer duration. As a result, LMFP-80 has the largest impedance by the end of charge before blocking conditions become dominant (0.37 Ω g), followed by LMFP-60 (0.28 Ω g) and LMFP-40 (0.17 Ω g). The end of the charge curve displays a more rapid increase in impedance, indicative of transport limitations when Li inventory is severely limited. When discharge begins, Mn^{3+} reduction starts with a higher impedance than the beginning of Mn^{2+} oxidation (Fig. 5c). These values correlate to the endpoint impedance values of Mn^{2+} oxidation. Similar to $Fe^{2+/3+}$ redox, the values of impedance during Mn^{3+} reduction increase with Mn content: 0.12 Ω g for LMFP-40, 0.20 Ω g for LMFP-60, and 0.25 Ω g for LMFP-80. In contrast to oxidation, the impedance during reduction maintains a steady value during the entire reduction reaction, revealing that Mn^{3+} reduction does not become more resistive as the reaction proceeds. Therefore, the kinetics of $Mn^{2+/3+}$ redox couple is asymmetric. Furthermore, Mn^{2+} oxidation should be treated as the rate limiting reaction of any LMFP system due to increasing impedance and its impact on the impedance of Mn^{3+} reduction.

The kinetic limitations of Mn^{2+} oxidation are constituted of multiple underlying mechanisms. First, the formation of Mn^{3+} instigates Jahn–Teller distortion. As more Mn^{3+} is formed, the increase in the Jahn–Teller active ion results in increased lattice strain on the MFP structure, causing the oxidation reaction to become more resistive as it proceeds. In addition to the impacts of Jahn–Teller distortion, Mn^{2+} oxidation forms MFP, a charge-transfer insulator.[40] Assuming that Fe and Mn are homogeneously distributed in LMFP, the first particle to undergo Mn^{2+} oxidation takes place on the surface of the cathode. The reaction front then proceeds from the surface of the particle into the bulk, represented as a core–shell model.[1,21]

Once the surface is covered by the charge-transfer insulating MFP phase, progression of the reaction front into the bulk becomes restricted. Conversely, Mn^{3+} reduction forms partially lithiated LMFP phase on the surface, reducing the energy barrier for Li migration.[38,39] Therefore, Mn^{3+} reduction reaction front can proceed into the bulk of the material without hindrance. Scheme 1 presents the asymmetric $Mn^{2+/3+}$ redox couple within the LMFP lattice.

Correlating these conclusions to the *operando* GEIS data explains the limited electrochemical performance of LMFP-80. LMFP-80 has the highest impedance of all cathodes tested because it undergoes Mn^{2+} oxidation for the longest duration. Therefore, the linear increase in impedance lasts longer than that of LMFP-40 and LMFP-60, forcing LMFP-80 to high impedance values by the end of charge. LMFP-80 has the most severe lattice strain, due to a high concentration of Jahn–Teller active Mn^{3+}, in its charged state. Therefore, the subsequent Mn^{3+} reduction reaction in LMFP-80 has high impedance because of the high-strain structure that Mn^{2+} oxidation formed. While Mn^{2+} oxidation is the culprit for high impedance of LMFP-80, the entire redox couple demonstrates high impedance that cannot be reduced to match those of LMFP-40 and LMFP-60. Notably, the linear impedance increase of Mn^{2+} oxidation is present in all LMFP symmetric cells presented previously (Fig. 4a), signifying the validity of *operando* GEIS across symmetric and full cells.

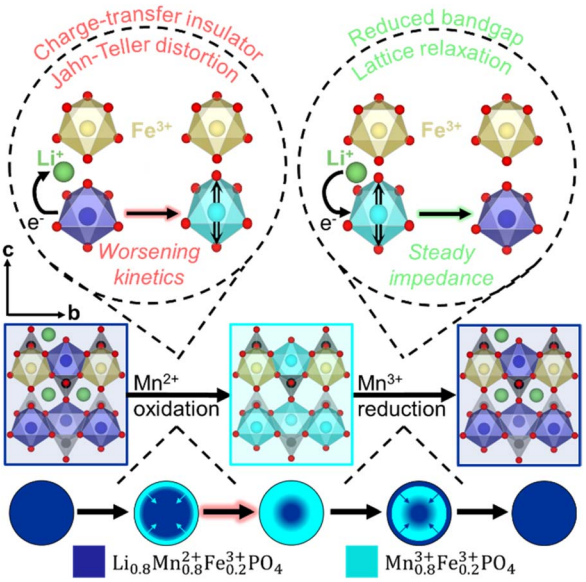

Scheme 1 Particle and lattice structures of LMFP-80 during Mn^{2+} oxidation and Mn^{3+} reduction. The red arrow in the series of steps, presenting the core–shell behavior of the LMFP-80 particle, indicates the slowest step of $Mn^{2+/3+}$ redox: the diffusion of Li across the delithiated, charge insulative MFP phase.

Another variable that could aid in alleviating the kinetic limitations of $Mn^{2+/3+}$ redox is elemental doping. A wide range of elements have been doped into LMFP to improve its electrochemical performance.[17,26,32,41] Each study has concluded that the benefits of doping, including but not limited to, alleviating Jahn–Teller distortion, increasing electrical conductivity, and widening the Li ion-transfer channels along the *b* axis, improve the performance of LMFP compared to an undoped baseline. For this study, three dopants were included in the LMFP cathodes: Co, V, and Mg. As mentioned previously, Co assists in the graphitization of the organic carbon sources to form a conductive carbon coating on the LMFP particles, thereby increasing the electrical conductivity of the active material. The addition of V addition forms $Li_3V_2(PO_4)_3$, which exhibits fast Li^+ diffusion. Mg acts as a pillaring ion that provides crystalline structure stabilization during Jahn–Teller distortion. Each of these three dopants improves the kinetics of LMFP.[17,25,42] Thus, potential improvements in kinetics through doping have been achieved and accounted for in our samples. However, despite engineering the LMFP cathode with this carefully designed combination of dopants, the impedance of LMFP-80 remains significantly higher than that of LMFP-40 and LMFP-60. The drawbacks of high-Mn LMFP compositions like LMFP-80 cannot be easily resolved by doping, and further research into the kinetics of these cathodes is needed before their practical application.

Conclusions

The electrochemical performance of the $Mn^{2+/3+}$ redox couple in LMFP is the major determinant of the energy the cathode can obtain. Overall, this study probed this redox couple with emphasis on discovering the conditions that best enable a full utilization of the $Mn^{2+/3+}$ redox. Both LMFP symmetric cells and LMFP‖LTO full cells examined the rate capabilities and impedance of the cathode material without impedance contributions from other factors, such as from a Li metal anode. Restricted rate capability and high impedance occur in LMFP-80. While increasing the cycling temperature and decreasing the current reduce the impedance of the systems with moderate Mn content, these changes cannot impactfully remedy the extremely high impedance of LMFP-80. *Operando* GEIS indicates that Mn^{2+} oxidation grows more resistive as the reaction occurs, while Mn^{3+} reduction holds constant impedance. Therefore, the resistance of the Mn^{2+} oxidation reaction is the culprit of the kinetic limitations of LMFP. With respect to electric vehicles, monitoring the charge rate during the Mn^{2+} oxidation reaction is necessary to maximize the range of the vehicles. It is suggested that for the best application, Mn content in LMFP should not be near 80% Mn as the impedance for these systems severely hinders the performance of the cathode. In order to achieve the optimal energy density with LMFP, moderate Mn content should be pursued.

Author contributions

S. R. conceptualized the project idea and developed the methodology. S. R. performed the material preparation, electrochemical testing, and structural and spectroscopic characterizations. All the authors wrote the manuscript. A. M. supervised the research.

Conflicts of interest

There are no conflicts to declare.

Data availability

The authors used available software to analyze the impedance data using the Distribution of Relaxation Time (DRT) method.[35] Any additional information is available from the authors upon request.

Additional characterization and electrochemical data supporting this article have been included as part of the SI. See DOI: **https://doi.org/10.1039/d5ta05970d**.

Acknowledgements

This work was supported by the U. S. Department of Energy, Office of Basic Energy Sciences, Division of Materials Science and Engineering under award number DE-SC0005397. One of the authors (S. R.) thanks the National Science Foundation for the award of a graduate fellowship. The authors thank Kevin Scanlan and Seamus Ober for insightful discussions.

References

1 A. K. Padhi, K. Nanjundaswamy and J. Goodenough, *J. Electrochem. Soc.*, 1997, **144**, 1188.
2 S. Y. Chung, J. T. Bloking and Y. M. Chiang, *Nat. Mater.*, 2002, **1**, 123–128.
3 A. Yamada, S. C. Chung and K. Hinokuma, *J. Electrochem. Soc.*, 2001, **148**, A224.
4 P. P. Prosini, M. Carewska, S. Scaccia, P. Wisniewski and M. Pasquali, *Electrochim. Acta*, 2003, **48**, 4205–4211.
5 W. J. Zhang, *J. Power Sources*, 2011, **196**, 2962–2970.
6 W. Li, E. M. Erickson and A. Manthiram, *Nat. Energy*, 2020, **5**, 26–34.
7 S. Lee, K. Scanlan, S. Reed and A. Manthiram, *Adv. Energy Mater.*, 2024, **15**, 2403002.
8 E. Lyle, R. Vaeli, A. Dutta and M. Metzger, *J. Electrochem. Soc.*, 2022, **169**, 060526.
9 D. B. Ravnsbæk, K. Xiang, W. Xing, O. J. Borkiewicz, K. M. Wiaderek, P. Gionet, K. W. Chapman, P. J. Chupas, M. Tang and Y. M. Chiang, *Nano Lett.*, 2016, **16**, 2375–2380.
10 T. Muraliganth and A. Manthiram, *J. Phys. Chem. C*, 2010, **114**, 15530–15540.
11 S. Reed, K. Scanlan and A. Manthiram, *J. Mater. Chem. A*, 2024, **12**, 21341–21349.
12 P. Vanaphuti, K. Scanlan and A. Manthiram, *RSC Sustainability*, 2024, **2**, 1969–1978.
13 A. Yamada, Y. Takei, H. Koizumi, N. Sonoyama, R. Kanno, K. Itoh, M. Yonemura and T. Kamiyama, *Chem. Mater.*, 2006, **18**, 804–813.
14 E. Xu, T. Wang, J. Chen, J. Hu, H. Xia, H. Wu, W. Cai, Q. Zhang, Y. Zhang and K. Wu, *Adv. Energy Mater.*, 2024, **15**, 2404929.
15 B. Kang and G. Ceder, *J. Electrochem. Soc.*, 2010, **157**, A808.
16 D. B. Ravnsbæk, K. Xiang, W. Xing, O. J. Borkiewicz, K. M. Wiaderek, P. Gionet, K. W. Chapman, P. J. Chupas and Y. M. Chiang, *Nano Lett.*, 2014, **14**, 1484–1491.
17 P. Vanaphuti and A. Manthiram, *Small*, 2024, **20**, 2404878.
18 S. Wi, J. Park, S. Lee, J. Kim, B. Gil, A. J. Yun, Y. E. Sung, B. Park and C. Kim, *Nano Energy*, 2017, **39**, 371–379.
19 J. Kim, Y.-U. Park, D.-H. Seo, J. Kim, S.-W. Kim and K. Kang, *J. Electrochem. Soc.*, 2011, **158**, A250.
20 J. Yang, C. Li, T. Guang, H. Zhang, Z. Li, B. Fan, Y. Ma, K. Zhu and X. Wang, *Nano Lett.*, 2021, **21**, 5091–5097.
21 C. Delmas, M. Maccario, L. Croguennec, F. Le Cras and F. Weill, *Nat. Mater.*, 2008, **7**, 665–671.
22 E. Lyle, R. Vaeli, M. Cormier and M. Metzger, *J. Electrochem. Soc.*, 2022, **169**, 060527.
23 S. K. Martha, O. Haik, E. Zinigrad, I. Exnar, T. Drezen, J. H. Miners and D. Aurbach, *J. Electrochem. Soc.*, 2011, **158**, A1115.
24 A. Oya, R. Yamashita and S. Otani, *Fuel*, 1979, **58**, 495–500.
25 L. Wu, J. Lu, G. Wei, P. Wang, H. Ding, J. Zheng, X. Li and S. Zhong, *Electrochim. Acta*, 2014, **146**, 288–294.
26 H. Yu, E. Zhang, J. Yu, S. Yu, Y. Fang, L. Chen, H. Jiang and C. Li, *J. Mater. Chem. A*, 2024, **12**, 26076.
27 L. Minnetti, V. Marangon and J. Hassoun, *Adv. Sustainable Syst.*, 2022, **6**, 2100464.
28 K. Scanlan and A. Manthiram, *Electrochim. Acta*, 2025, **520**, 145875.
29 R. Tian, P. J. King, J. Coelho, S. H. Park, D. V. Horvath, V. Nicolosi, C. O'Dwyer and J. N. Coleman, *J. Power Sources*, 2020, **468**, 228220.
30 W. Yang, Y. Bi, Y. Qin, Y. Liu, X. Zhang, B. Yang, Q. Wu, D. Wang and S. Shi, *J. Power Sources*, 2015, **275**, 785–791.
31 N. N. Bramnik, K. G. Bramnik, K. Nikolowski, M. Hinterstein, C. Baehtz and H. Ehrenberg, *Electrochem. Solid-State Lett.*, 2005, **8**, 6–9.
32 J. Huang, X. Tang, Y. Zhou, T. Wang, F. Zhao, W. Wang, Y. Meng, W. Cen and Y. Zhang, *J. Mater. Chem. A*, 2025, **13**, 10550–10560.
33 K. P. Scanlan and A. Manthiram, *J. Electrochem. Soc.*, 2023, **170**, 100515.
34 A. Maradesa, B. Py, J. Huang, Y. Lu, P. Iurilli, A. Mrozinski, H. M. Law, Y. Wang, Z. Wang, J. Li, S. Xu, Q. Meyer, J. Liu, C. Brivio, A. Gavrilyuk, K. Kobayashi, A. Bertei, N. J. Williams, C. Zhao, M. Danzer, M. Zic, P. Wu, V. Yrjänä, S. Pereverzyev, Y. Chen, A. Weber, S. V. Kalinin, J. P. Schmidt, Y. Tsur, B. A. Boukamp, Q. Zhang, M. Gaberšček, R. O'Hayre and F. Ciucci, *Joule*, 2024, **8**, 1958–1981.
35 F. Ciucci, A. Maradesa and Y. Wang, DRT-Survey, 2024, **https://github.com/ciuccislab/DRT-Survey**.
36 A. C. Lazanas and M. I. Prodromidis, *ACS Meas. Sci. Au*, 2023, **3**, 162–193.
37 N. Meddings, M. Heinrich, F. Overney, J. S. Lee, V. Ruiz, E. Napolitano, S. Seitz, G. Hinds, R. Raccichini, M. Gaberšček and J. Park, *J. Power Sources*, 2020, **480**, 228742.
38 M. Yao, Y. T. Wang, J. A. Chen, H. Dong, M. Li, X. Zhang, C. Wang, G. Huang and S. Xu, *ACS Appl. Mater. Interfaces*, 2024, **16**, 66077–66088.
39 D. Kwon and D. Kim, *Adv. Energy Mater.*, 2025, **15**, 2501444.
40 M. K. Kinyanjui, P. Axmann, M. Wohlfahrt-Mehrens, P. Moreau, F. Boucher and U. Kaiser, *J. Phys.: Condens. Matter*, 2010, **22**, 275501.
41 J. Han, J. Zhu, X. He, M. Yang, C. Yan, D. Ma, L. Zhang and P. Zhang, *ACS Appl. Mater. Interfaces*, 2025, **17**, 32381–32391.
42 W. Xiang, Y. Zhong, Y. Tang, H. Shen, E. Wang, H. Liu, B. Zhong and X. Guo, *J. Alloys Compd.*, 2015, **635**, 180–187.